Two-photon laser spectroscopy of xenon collision pairs

T. D. Raymond,* N. Böwering, Chien-Yu Kuo,† and J. W. Keto
Physics Department, University of Texas at Austin, Austin, Texas 78712
(Received 13 June 1983)

A computer-controlled, frequency-doubled, pulsed dye laser has been used in conjunction with a sensitive and linear photodetection scheme to measure the two-photon absorption profiles of the ground to $6p[\frac{1}{2}]_0$, $6p[\frac{3}{2}]_2$, and $6p[\frac{5}{2}]_2$ two-photon transitions in xenon over a pressure range of a few Torr to 10 000 Torr. Absolute two-photon coefficients are reported. Line-shape measurements of the shift and width of the Lorentzian core allow the deduction of the long-range dispersion terms of the Xe-Xe* interaction potentials. An analysis of the line wings under the quasistatic approximation has permitted the extraction of the difference potentials for $3.75 \leq R \leq 8.0$ Å. These short- and long-range difference potentials have been combined and used in an Anderson-Talman phase-shift calculation to reconstruct the absorption profiles. Measurements of the fluorescence following selective laser excitation have been taken and branching fractions for collisional excitation to other members of the $6p$ manifold at a xenon pressure of 100 Torr are reported.

I. INTRODUCTION

During the past decade several detailed spectroscopic studies of the excited-state configurations of xenon atoms and dimers have been undertaken using optical excitation techniques. While the $5p^5 6s$ and $5p^5 6s'$ configurations were examined by numerous investigators using discharge lamps or synchrotron radiation,[1,2] only a few experiments on the higher-state configurations $5p^5 6p$ and $5p^5 5d$ have been reported. Castex[1] has observed molecular absorption bands in this region corresponding to collision-induced dipole transitions in single-photon experiments. Margani *et al.*[3] investigated the near-infrared emission of xenon $6p$-$6s$ transitions following vacuum-ultraviolet (vuv) excitation. The states of the $5p^5 6p$ manifold are of particular interest because they are populated rapidly by dissociative recombination at higher pressures, and little is known about the potential surfaces and collision pairs formed at high pressures. The advent of tunable dye lasers has stimulated experiments using multiphoton excitation. The advantages of this technique are numerous: selective excitation is possible with high resolution, absorption lengths are suitably large at high pressures, and larger multiplicities can be excited. For allowed dipole-dipole transitions, two-photon excitation is complementary to single-photon excitation since levels in different configurations and symmetries are excited. In two-photon dipole-dipole transitions the Xe $5p^5 6p$ atomic configuration is accessible from the ground state and the corresponding molecular states are of *gerade* symmetry. Hawkins *et al.*[4] obtained the first two-photon absorption spectra of xenon. Gornik and co-workers[5] have examined two-photon transitions to the $6p[\frac{1}{2}]_0$, $6p[\frac{3}{2}]_2$, $6p[\frac{5}{2}]_2$, $5d[\frac{7}{2}]_3$, and $5d[\frac{5}{2}]_3$ atomic levels as well as the $0g^+(^3P_1)$, $1g(^3P_1)$, and $1g(^3P_2)$ molecular states of the $5p^5 6s$ configuration. We report here precise measurements of the self-broadened absorption line profiles of the atomic states dissociating to the $6p$ manifold as obtained from laser-induced fluorescence (LIF) with Doppler-free two-photon excitation.[6] We also report an analysis of the branching ratios of the resultant fluorescence.

A description of the experimental apparatus is given in Sec. II of this paper. Levels in the energy region of 77 000 to 81 000 cm^{-1} above the ground state are excited with a frequency-doubled dye laser in the pressure range from 1 to 10 000 Torr (see Fig. 1). To obtain excitation spectra we scan the laser frequency and monitor the fluorescence at one of the various near-infrared transitions between atomic $6p$ and $6s$ states while simultaneously recording radiation of excimers at 1730 Å in the vuv. The fluorescence spectra are obtained by keeping the laser frequency fixed and scanning either the infrared (ir) or vacuum-ultraviolet (vuv) monochromator. In Sec. III measurements at low pressures are reported and two-photon excitation cross sections are deduced. In Sec. IV the line profiles of excited $6p$ states are analyzed in detail to extract the potential curves of dimers associated with these levels. The broadening of the line core at low pressures is used to determine the dominating long-range interaction term. Modeling of the line wings at higher pressures yields information on the potentials at all internuclear separations accessible in this experiment. Section V deals with fluorescence spectra obtained by varying the detection wavelength at fixed laser frequency to study collisional excitation transfer. We determine branching fractions for collisional energy transfer from the $6p[\frac{1}{2}]_0$, $6p[\frac{3}{2}]_2$, and $6p[\frac{5}{2}]_2$ states to other $6p$ manifold states.

II. EXPERIMENTAL APPARATUS

A high-power nitrogen laser[7] is used to pump an amplified dye laser[8] containing Coumarine 500 (see Fig. 2). The oscillator is a 40-cm-long cavity containing a 20× prism beam expander, a 316-groove/mm echelle grating mounted on a "broken sine bar drive," and an optional piezoelectrically driven Fabry-Perot etalon. The grating drive and

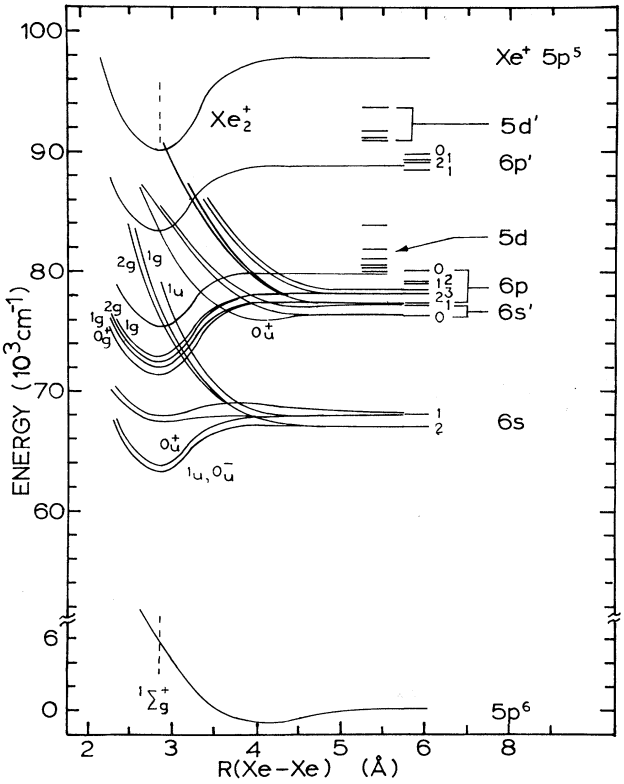

FIG. 1. States of the 6*p* manifold are excited via two-photon absorption. The molecular curves drawn are based on the estimates by Mulliken (Ref. 23).

etalon are computer controlled. Without the etalon, the laser linewidth is about 0.08-Å FWHM (full width at half maximum) and the smallest scan step is 0.074 Å ; with the etalon, the linewidth is reduced to 500 MHz with a 25 MHz minimum step size. We have not measured the linewidths after frequency doubling but estimate them, according to the results of Ref. 4, to be one-half that of the visible laser. The oscillator output is highly linearly polarized with a Glan Air polarizer used in conjunction with the prism beam expander. This beam is spatially filtered and amplified in a single pass amplifier. The amplifier output consists of a 4-ns FWHM pulse with peak power up to 60 kW without and 25 kW with the etalon. The spatial distribution of the output beam was measured to be Gaussian-type in both vertical and horizontal directions. The profiles were measured during a single laser shot using a diode array and were found to be stable on a shot-to-shot basis.

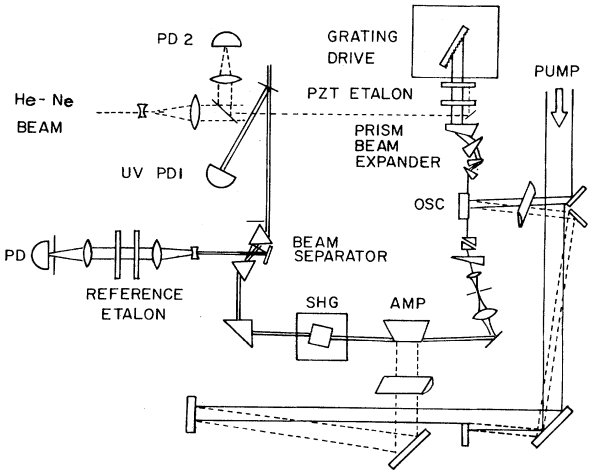

FIG. 2. A Hänsch-type nitrogen laser pumped dye laser is frequency doubled in LFM to produce 100-W, 3-ns, and 500-MHz pulses at about 40 000 cm^{-1} with a repetition rate of 30 Hz. A set of external etalons sample the laser fundamental to provide a frequency reference. A calibrated photodiode PD1 is used to obtain a shot-by-shot laser power measurement to which the induced fluorescence is normalized.

In the narrow-band configuration, the laser frequency is tuned by scanning the etalon over one free-spectral range at a time and simultaneously using the grating to pick successive etalon orders. The use of piezoelectric scanning introduced problems associated with their inherent drift and hysteresis.[9] The hysteresis problem is overcome by the use of a voltage ramping routine incorporating fixed voltage endpoints, unidirectional scanning, and a 60-sec pause at one endpoint.[8] In this manner it is possible to scan several etalon free-spectral ranges without frequency discontinuities at the etalon turning points. The drift problem is handled by the use of external reference etalons. These etalons consist of a 3-GHz free-spectral range, confocal etalon of finesse 100 and a 15-GHz Fabry-Perot etalon of finesse 30. These etalons are housed in a thermally isolated box and serve as absolute frequency markers.

The dye laser output is directed, unfocused, through a 10-mm cube of LFM (lithium formate monohydride) to produce radiation at the second harmonic. The fundamental power was typically reduced to produce uv pulses of less than 100-W peak power (3-ns FWHM) in order to minimize damage to the LFM crystal as well as to avoid saturation of the transition, photoionization of the excited state, and stimulated emission from the 6*p* state to the lower-lying 6*s* states.[10] The combination of Coumarine 500 and LFM crystal allowed the production of uv radiation from about 2450 Å to about 2600 Å . The second harmonic is separated from the fundamental by means of two counteracting Brewster angle prisms. Because the uv light is linearly polarized, the insertion loss of this filter is very low; furthermore, the fact that the dispersions of the two prisms counter one another means that the wavelength dependence of the angular deviation of the beam is eliminated. An uncoated MgF_2 slab reflects a small fraction of the uv light onto an absolutely calibrated *p-i-n* photodiode (EG&G FND100), shown as PD1 in Fig. 2. The laser beam is deflected by a small diameter mirror onto a 100-mm focal length Suprasil lens which focuses the light into the chamber. The focal spot is approximately 15 μm in diameter yielding a power density from 1 to 60 MW/cm^2. Upon exiting the chamber, the laser beam is reflected and refocused by a concave spherical mirror such that the counter-propagating beams have overlapping focal spots.

The gas used in this experiment was commercially obtained high-purity xenon (Airco 99.997%). This sample was further purified by passing it over a titanium sponge

held at 300°C. The gas handling system and the sample chamber, built to uhv standards, were baked to 300°C and evacuated to 5×10^{-8} Torr for four days prior to the introduction of the gas. The sample chamber, shown in Fig. 3, is capable of withstanding pressures greater than 10000 Torr. The pressure is monitored by 10- and 10000-Torr capacitance manometers with an accuracy of 0.1%. The pressure is easily varied by the use of a cryotip cooled by liquid nitrogen. The windows used for the laser beam and near-infrared fluorescence collection are MgF_2 antireflection coated sapphire sealed with gold *O*-rings. At a right angle to this optic axis is a LiF window brazed to a conflat flange that permits the observation of the vuv fluorescence. The sapphire windows are aligned with their optic axis along the direction of polarization of the laser.

The fluorescence in the near infrared (ir) is detected with a computer-controlled 1-m Jobin-Yvon monochromator whose optic axis coincides with the laser beam. The mirror used to reflect the laser into the chamber is small enough so as to obstruct only a small fraction of the radiation emanating from within the chamber. This mirror is positioned to prevent fluorescence from the sapphire windows and Suprasil lens from entering the monochromator. Residual fluorescence produced a maximum of one count per 100 laser shots. The grating used has 600 grooves/mm and was operated in third order. The radiation is detected with an RCA 8852 photomultiplier cooled to −25°C to minimize the dark current. The overall detection efficiency, as measured against tungsten lamp traceable to National Bureau of Standards (NBS), varied from about 5.6×10^{-4} at 8000 Å to 6.6×10^{-6} at 9165 Å.

The vuv fluorescence is collected at a right angle to the laser beam with a computer-controlled 1-m monochromator.[11] The radiation was detected with a sodium salicylate-photomultiplier combination. The lower level of detection was limited by scattered laser light to about the same noise level as in the near infrared. The overall collection efficiency was estimated to be 8×10^{-6} at 1730 Å. The optical path through the xenon sample in the direction of the vuv monochromator is quite long (20 cm) causing resonance absorption of all resonant transitions. This prevented the detection of any of the atomic resonance lines; the observable vuv radiation originated from transitions from the lowest-lying excimers to the repulsive part of the ground state (approximately 1730 Å). At pressures below 1000 Torr excitation spectra are reported only in the ir. Above 1000 Torr, $6s'[\frac{1}{2}]_0$ and $6s[\frac{3}{2}]_1$ are rapidly quenched by formation of $^{1,3}\Sigma$ excimers. The slower decaying state, $6s[\frac{3}{2}]_1$, has a lifetime of only 11 ns at 1000 Torr[2]; hence, little diffusion of the excited species is expected and the vuv fluorescence at 173 nm is an accurate measure of the total two-photon absorption rate.

The use of a Digital Equipment Corporation PDP11/34 minicomputer allows the data acquisition to be nearly fully automated. The computer is used not only to accumulate and process signals from the photomultipliers and photodiodes, but is also used to position and scan the laser and monochromator frequencies. A schematic diagram of the acquisition system is shown in Fig. 4.

The high power and short duration of the laser pulse together with the short lifetimes of the excited states create photon count rates that preclude the use of single photon counting techniques, particularly near the atomic resonances. To obtain a linear detection system throughout the spectral profile, a charge integration technique is used. The charge from the phototubes is integrated in an 11-bit (binary digits) charge digitizer for 100 ns following the laser excitation. The amount of charge corresponding to a single photoelectronic event is then used to calculate the number of photons detected. This technique has been verified to be linear up to 900 photoelectrons per gate period

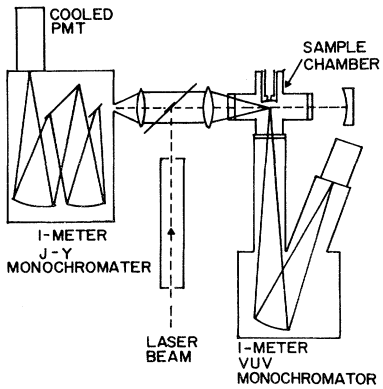

FIG. 3. High-purity xenon gas sample is contained in a stainless-steel, ultra-high-vacuum chamber. The laser enters the chamber by reflection from a small circular mirror evaporated on a glass substrate and is focused to a 15-μm diameter spot. Fluorescence in the infrared is observed along the laser axis while the fluorescence in the vacuum ultraviolet is observed at right angles to this axis.

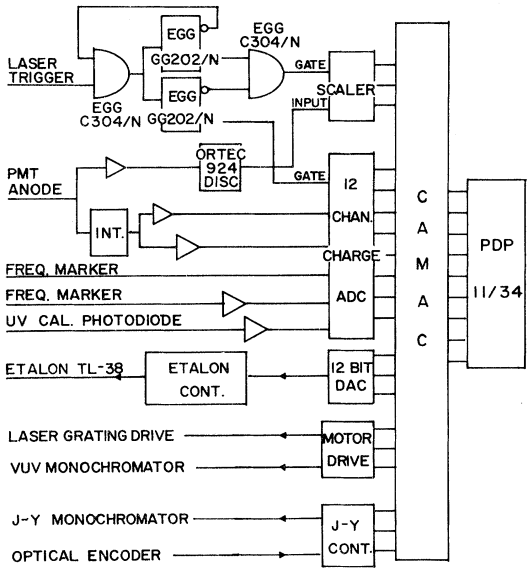

FIG. 4. A PDP-11/34 minicomputer collects the experimental data and controls the instruments via CAMAC interface. Input consists of fluorescence signals from the photomultipliers, laser power signal from the calibrated photodiode, and laser frequency information from diodes monitoring the transmission through the reference etalons. Control signals are applied to the laser grating drive, the intracavity etalon, and the monochromators.

[limited by the photomultiplier tube (PMT)] by monitoring Rayleigh scattered light versus laser power. In order to preserve accuracy for low count rates while maintaining linearity for high rates, two digitization channels are used. The high-gain channel corresponds to 0 to 45 photons full scale of the digitizer and the other to 0 to 900 photons full scale. After the first 100 ns the count rate is sufficiently low to allow single photon counting; a scalar is then used to count the photons that occur in the following 4.5 μs. The charge from the power diode PD1 is amplified and also digitized. The computer divides the fluorescence signals by the square of this value to eliminate shot-to-shot laser power fluctuations. Extreme laser power variations are eliminated through the use of a software discriminator that limits the acceptable laser power range. The precision of the entire system is about $\pm 5\%$.

III. OBSERVED SPECTRA

In Fig. 5 we show a broad excitation spectrum observed at 2800 Torr. To obtain this spectrum, the laser frequency of the broadband laser was scanned while the fluorescence was monitored at 1730 Å . On the abscissa the laser frequency is plotted, on the ordinate the fluorescence signal divided by the square of the laser power in arbitrary units. The bright features observed are two-photon allowed dipole-dipole transitions to $J=0$ and 2 states of xenon $5p^5 6p$. Arrows indicate the locations of $6p$ manifold members with forbidden (under present geometry) two-photon transitions. Surprisingly, at this pressure we do not observe collision-induced transitions to the gerade symmetries of excimers dissociating to these atomic levels. Only at pressures of 10 000 Torr do we see the first evidence of such transitions. Owing to their greater vuv sensitivity obtained by not using a monochromator, Gornik *et al.*[5] observed features in these spectral regions at much lower pressures; it is our belief that these features are evidence of such collision-induced transitions.[6] We also observe the dipole-quadrupole transition to $5d[\frac{7}{2}]_3$. The structure to the red of this atomic transition has been identified as excimer bands of this transition.[5] As explained in Sec. VI, we interpret the spectral feature near 39 800 cm^{-1} as collision-induced excitation near avoided crossings of attractive potentials of 1_g symmetries of $5d[\frac{1}{2}]_1$ and repulsive potentials of $6p[\frac{3}{2}]_1$.

Figure 6 shows the ir photosignal as a function of the

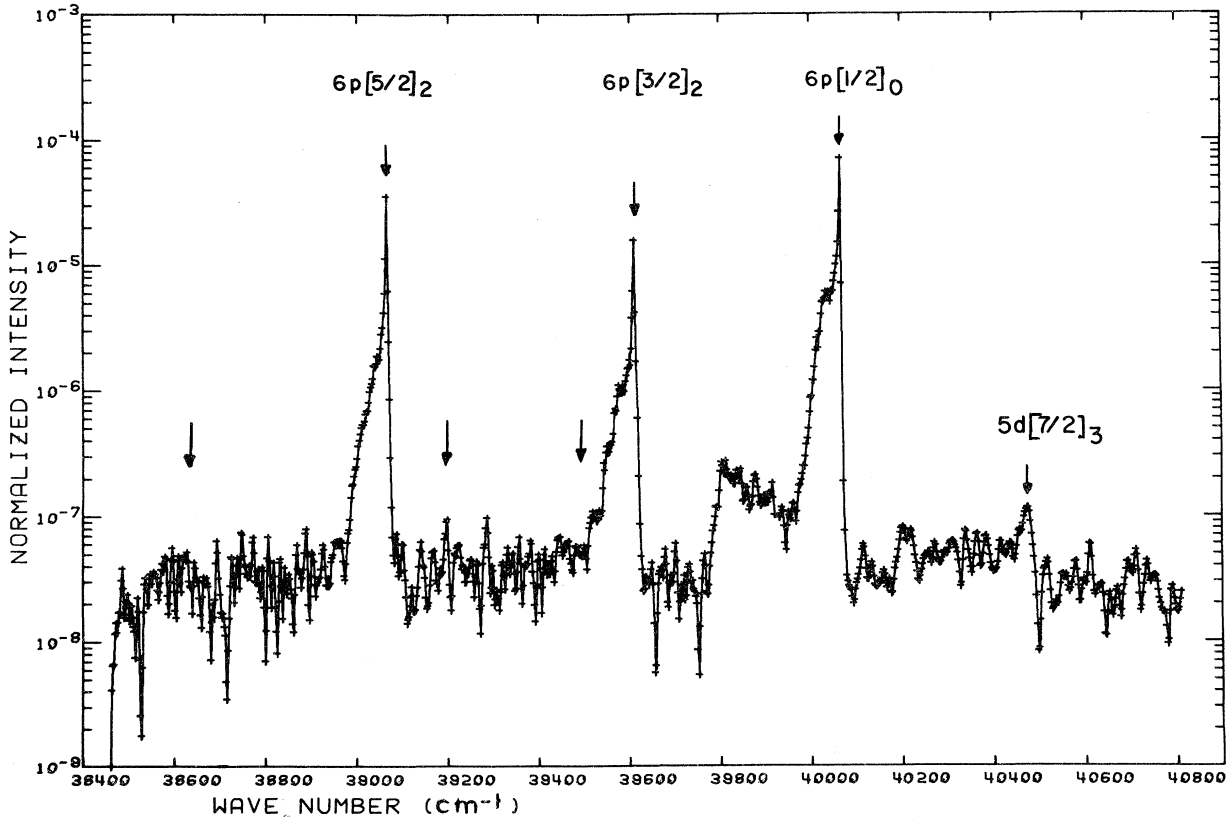

FIG. 5. Fluorescence signal at 1730 Å , normalized to the square of the laser power and averaged over 200 laser shots per point at a xenon pressure of 2800 Torr, is shown as a function of laser frequency. The units of the vertical scale are arbitrary. The large peaks correspond to the dipole-dipole allowed transitions. The small feature at about 40 450 cm^{-1} has been identified as a dipole-quadrupole transition to $5p[\frac{7}{2}]_3$ (Ref. 5), while we interpret the feature at 39 800 cm^{-1} as due to an avoided crossing between molecular curves from $5d[\frac{1}{2}]_1$ and $6p[\frac{3}{2}]_1$. The arrows indicate the frequencies of nonallowed two-photon transitions to the $J=1$ members of the $6p$ manifold. Only at pressures of about 10 000 Torr do the transitions to the molecular curves dissociating to these levels become evident.

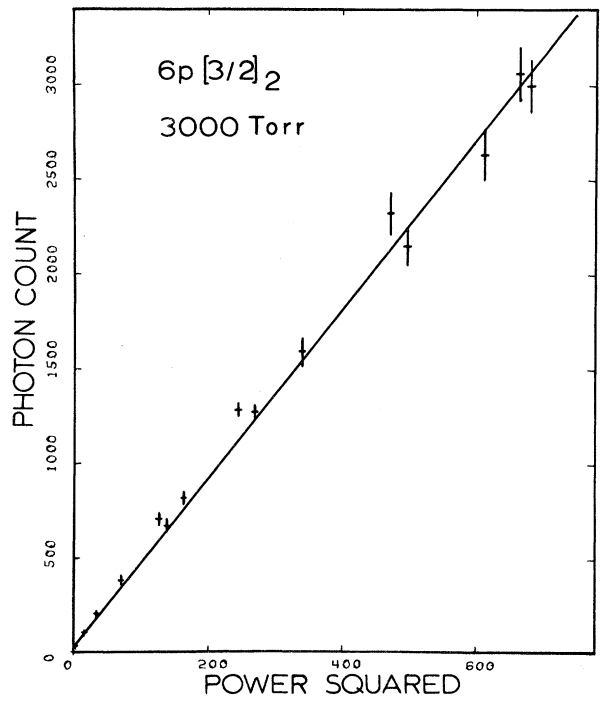

FIG. 6. Fluorescent intensity, in arbitrary units, is plotted against the square of the laser power, also in arbitrary units. The straight line behavior is characteristic of a two-photon absorption process.

laser power squared with the laser tuned to the atomic resonance of $6p[\frac{3}{2}]_2$ at a pressure of 2800 Torr; the linear dependence on this scale is the signature of a two-photon process. The onset of stimulated emission was easily observed since it caused enhanced core intensities of the line shapes, large fluctuations in the fluorescence intensity on a shot-to-shot basis, and deviations from a quadratic power dependence. At the lowest pressures laser powers of the order of 1 W were required to ensure against stimulated emission.

The two-photon transition rate on resonance, $R_{ge}(0)$, for dipole-dipole allowed transitions with counterpropagating beams of equal intensity I may be written in the form

$$R_{ge}(0)=6\alpha I^2 g(0)\,, \tag{1a}$$

where

$$g(0)=\begin{cases}\left[\dfrac{\pi}{2\ln 2}\right]^{1/2}\left[\dfrac{1}{\Delta\omega_1}+\dfrac{1}{(\Delta\omega_d^2+\Delta\omega_1^2)^{1/2}}\right], & \\ \qquad\qquad \gamma_e \ll \Delta\omega_1, \Delta\omega_d & \text{(1b)}\\ \dfrac{4}{\gamma_e}, \quad \gamma_e \gg \Delta\omega_1, \Delta\omega_d\,. & \text{(1c)}\end{cases}$$

γ_e denotes the natural width of the excited state, the laser bandwidth (FWHM in rad/s) is $\Delta\omega_1$, while the Doppler width (FWHM) is given by

$$\Delta\omega_d=(8\ln 2)^{1/2}\left[\frac{2\pi}{\lambda}\right]\left[\frac{2kT}{M}\right]^{1/2},$$

where M is the atomic mass and k is the Boltzmann constant. Here, the line-shape factors $g(0)$ are obtained by a convolution of the natural Lorentzian profile with the Doppler profile and the Gaussian profile of the laser. In Eq. (1a) we have a factor of 6 to account for the total intensity $4I_1I_2+I_1^2+I_2^2$ with $I_1=I_2=I$. From Ref. 12 we can derive the two-photon coefficient α to be

$$\alpha=\left[\frac{3\pi r_0 c}{\hbar}\right]^2\sum_i \frac{f_{gi}f_{ie}}{\omega_{gi}\omega_{ie}(\omega_1-\omega_{gi})^2} \times |\langle J_e 1 m_e 0\,|\,10\rangle\langle 1100\,|\,00\rangle|^2\,, \tag{2}$$

where m is the mass of the electron, r_0 is the classical electron radius, and J_e, m_e are the quantum numbers of the excited state. The oscillator strengths for transitions from the ground state to intermediate states and from the intermediate states to the excited state are given by f_{gi} and f_{ie}, respectively. The atomic energies of these states define the frequencies ω_{gi} and ω_{ie}; the laser frequency is ω_1 and its bandwidth is $\Delta\omega_1$. For a broadband laser the two-photon transition rate is independent of the natural width. In Table I we list the calculated transition rates for several intermediate states and the measured transition rates. The experimental cross sections have been measured using laser-induced fluorescence both in the ir and in the vuv. In the infrared, the optical detector system is absolutely calibrated using an NBS traceable standard lamp. In the vuv we have measured the two-photon coefficients at pressures of 1000–2800 Torr relative to the calculated Rayleigh scattering cross section[13] $d\sigma/d\Omega=6\times10^{-26}$ cm^{-2} for the scattering geometry, polarization, and laser frequencies of our experiment. This measurement does depend upon the relative efficiency of the optical system at the laser wavelength (250 nm) to the efficiency at the laser-induced fluorescence wavelength (173 nm). These are taken from the manufacturer's reflectance of the grating and literature values of relative efficiencies for the scintillator used as a detector. Since Rayleigh scattering is linear with laser power and two-photon LIF varies as the power squared, the relative measurement also depends upon the laser power and an average over the power distribution at the focus. The laser power was measured with an absolutely calibrated photodiode. The focal power distribution was estimated using a diode array. Final accuracy of the measurement by comparison to the Rayleigh scattering is ±50%. Cross sections measured in the infrared with lower pressures (a few Torr) are about an order of magnitude smaller than those measured in the vuv at the higher pressures. Since we expect these as well to be accurate to ±50%, we speculate that the LIF in the infrared is not isotropic; for the particular geometry used here, this could lead to a reduction in observed intensity. The power dependence was not explicitly tested *during* these measurements, although the power level was reduced sufficiently so that the line shape was not power dependent.

TABLE I. Estimated and measured two-photon coefficients α as defined by Eq. (2), for the xenon states $6p[\frac{1}{2}]_0$, $6p[\frac{3}{2}]_2$, and $6p[\frac{5}{2}]_2$. The single-path approximation is calculated using the oscillator strengths of Sabbagh and Sadeghi (Ref. 25). The Dirac-Fock summations were carried out by Pindzola *et al.* (Ref. 15). The experimentally measured values of Chen *et al.* (Ref. 14) and Gornik *et al.* (Ref. 5) are inferred from their measured transition rates. Gornik *et al.* (Ref. 5) report an uncertainty of a factor of 3 in their absolute measurements. The laser bandwidth for the experiment by Chen was assumed to be 0.01 Å.

	Xenon $6p$ two-photon coefficients α (cm^4/J^2)		
Excited state:	$6p[\frac{1}{2}]_0$	$6p[\frac{3}{2}]_2$	$6p[\frac{5}{2}]_2$
Theoretical values			
1. Single-path approximation			
$\|i\rangle$			
$6s[\frac{3}{2}]_1$	100	73	12
$5d[\frac{3}{2}]_1$	43	7.7	19
$7s[\frac{3}{2}]_1$	92	4.2	17
2. Dirac-Fock summations			
Dipole length	210		
Dipole velocity	58.9		
Experimental values			
1. Chen *et al.*	96		
2. Gornik *et al.*	108	12	61
3. This work	43±20	4.5±2	22±11

We observe *ratios* of two-photon coefficients listed in Table I of 8:4:1 for $6p[\frac{1}{2}]_0$:$6p[\frac{5}{2}]_2$:$6p[\frac{3}{2}]_2$. The accuracy of these relative rates is ±15%. These ratios are in significant disagreement with calculated ratios of 2.5:2:1 when using $6s[\frac{3}{2}]_1$ as the single intermediate state. We note in Table I that there should be a significant contribution to the theoretical transition rates from the $5d[\frac{3}{2}]_1$ and $7s[\frac{3}{2}]_1$ intermediate states; hence, a single intermediate-state model gives only an order-of-magnitude estimate and a sum over intermediate states is required for accurate calculations. Our measurements of the two-photon coefficients for the vuv are shown in Table I along with the measurements by Gornik *et al.*[5] and Chen *et al.*[14] and with the calculation by Pindzola *et al.*[15]

IV. LINE-SHAPE ANALYSIS

An extensive literature has been developed over the last three decades for the analysis of spectral line shapes associated with single photon transitions.[16] These theories may be applied to two-photon absorption if the intermediate-state detuning is large enough to preclude stepwise excitation;[12] such is the case for the $6p$ manifold of xenon as this detuning is greater than 26000 cm^{-1} (see Fig. 7). The two-photon absorption spectra for the dipole-dipole allowed transitions to the $6p$ manifold have been analyzed in the impact and static limits[17] and as well with the Anderson-Talman theory.[18]

A high-resolution excitation spectrum of the $6p[\frac{1}{2}]_0$ state of xenon at 400 Torr is shown in Fig. 8. The solid curve is a least squares fit of an asymmetric Lorentzian to the data. The impact limit of the unified Franck-Condon theory of Szudy and Baylis[17] has been applied. This theory

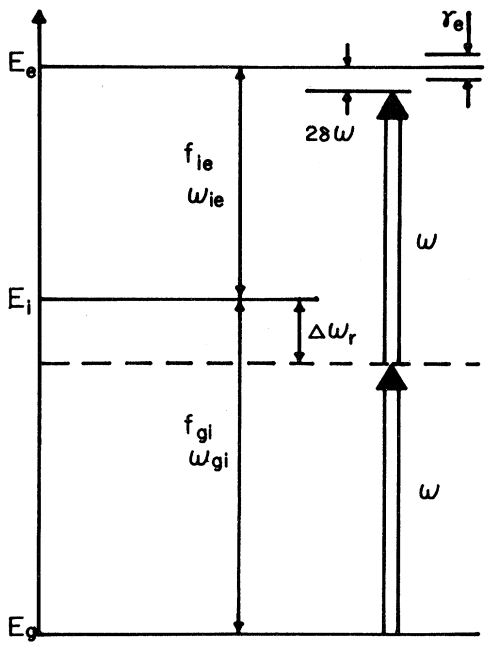

FIG. 7. Two-photon absorption process involves the absorption of two photons of frequency ω_1 to excite the state $|e\rangle$. The intermediate state $|i\rangle$ is dipole coupled to both the ground state, $|g\rangle$, and $|e\rangle$. The laser frequency is about 40000 cm^{-1} and is far from being resonant with $|i\rangle$ (the closest such state is $6s[\frac{3}{2}]_1$ which lies at 68000 cm^{-1}).

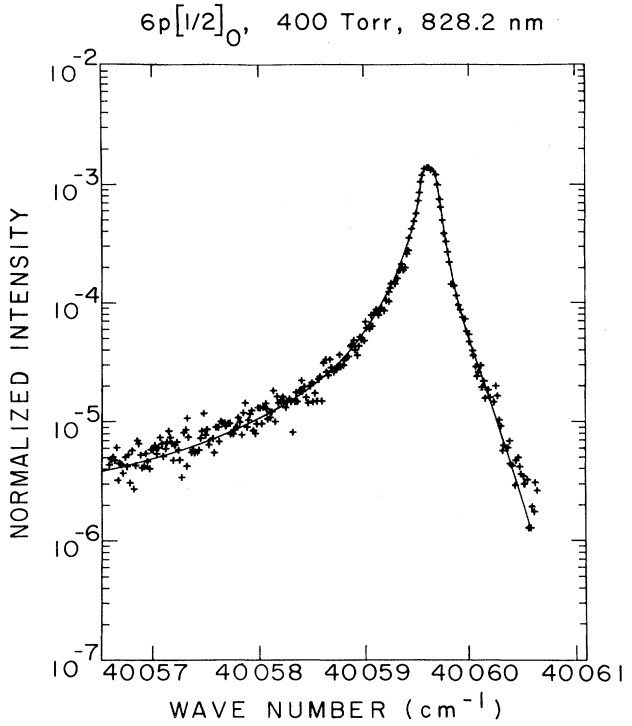

FIG. 8. Narrow-band laser was used to obtain this excitation spectrum of $6p[\frac{1}{2}]_0$ at 400 Torr. The transition of this state to the lower-lying $6s[\frac{3}{2}]_1$ state (8282 Å) was used as the fluorescence monitor. The solid curve is the least-squares fit of an asymmetric Lorentzian to the data.

predicts an asymmetric Lorentzian profile of constant asymmetry κ, full width at half maximum γ, and shift Δ. In this approximation, the two-photon transition rate R_{ge} for the case when $\gamma \gg \Delta\omega_1$, $\delta\omega_d$ is then given by

$$R_{ge}=6\alpha I^2\frac{\gamma[1+\kappa(2\delta\omega-\Delta)]}{(2\delta\omega-\Delta)^2+(\gamma/2)^2}\ , \tag{3}$$

where α is the two-photon coefficient defined in Eq. 2 and $\delta\omega=\omega_{ge}/2-\omega_1$ (see Fig. 7). Assuming that the long-range *difference* potential between the ground and excited states is expressible as an inverse power of R with exponent m and coefficient ΔC_m, then from Szudy and Baylis

$$\Delta=n_0 v D_3(m)\left[\frac{\Delta C_m}{v}\right]^{2/(m-1)}\ , \tag{4}$$

$$\gamma=n_0 v D_2(m)\left[\frac{\Delta C_m}{v}\right]^{2/(m-1)}\ , \tag{5}$$

and

$$\kappa=\frac{D_1(m)}{v}\left[\frac{\Delta C_m}{v}\right]^{1/(m-1)}\ , \tag{6}$$

with n_0 being the ground-state number density, v the mean relative velocity and $D_1(m)$, $D_2(m)$, and $D_3(m)$ being constants dependent on the power m of the long-range difference potential.[6,17] It is important to note that because of the nonzero asymmetry, Δ is not the shift of the maxima of the Lorentzian.

The experimentally observed shifts, widths, and asymmetries are consistent with this model when the difference potential is chosen as $\Delta C_5/R^5$ for the $J=2$ states and $\Delta C_6/R^6$ for the $J=0$ state. The interaction that varies as R^{-5} represents a resonant quadrupole-quadrupole interaction and is zero between states of $J=0$.[19] The values of Δ and γ, as extracted from least-squares fits to the data, are plotted as a function of pressure in Fig. 9 for each of the dipole-dipole allowed transitions; the values of ΔC_m were determined from the slopes of these shifts and widths. The long-range coefficients for the excited states are listed in Table II; the coefficient for $6p[\frac{1}{2}]_0$ has been corrected for the xenon ground-state contribution by using the C_6 term taken from the potential given by Barker *et al.*[20]; no correction is required for the C_5 terms as the ground state has no such contribution.

The line wings were studied with the broadband laser. Excitation spectra at 2800 Torr are shown in Fig. 10. The fluorescence from the xenon second continuum at 1730 Å was used as the monitor. The wings have distinct shoulders at about 100 cm^{-1} (atomic energy) from the the atomic peaks and the blue wings are very steep. Two static theories have been applied to the line wings of this high-pressure data to extract information regarding the interaction potentials at internuclear separation down to 3.75 Å.

In the quasistatic theory the quantum-mechanical dis-

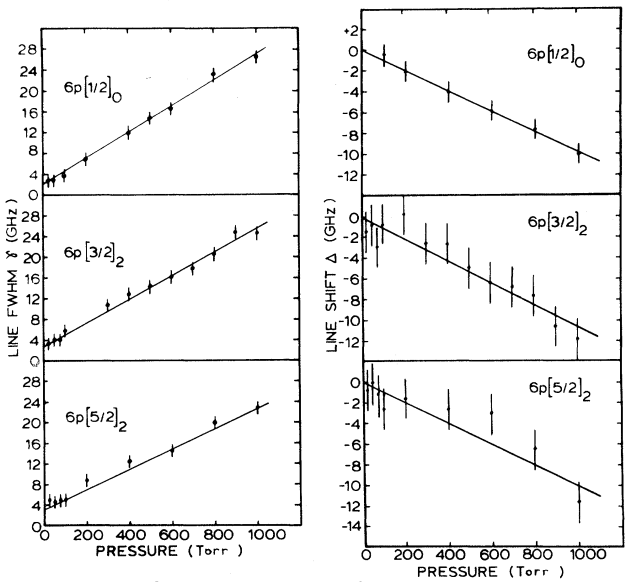

FIG. 9. Shift Δ and width γ of the low-pressure excitation spectra are plotted as a function of pressure for each of the dipole-dipole allowed transitions. These values were obtained by least-squares fitting the two-photon excitation spectra, such as that of Fig. 8, with an asymmetric Lorentzian. The linear dependence indicates that the impact approximation is valid for pressures at least to 1000 Torr.

TABLE II. Parameters for the difference potentials as estimated using the impact and quasistatic approximations. The impact approximation was used to extract the leading term of the long-range difference potentials; the long-range upper-state potential coefficients are obtained by adding the appropriate coefficients from the ground-state potential of Barker (Ref. 20). The values of the upper-state potentials as measured by Gornik (Ref. 5) are also listed. The short-range potential was extracted using the quasistatic approximation and the assumption that the difference potentials are all monotonic for $R > 3.75$ Å. The short-range difference potentials are given in terms of the coefficients of a sixth-order polynomial; the coefficients were obtained by least-squares fitting the polynomial to the numerically extracted difference potential. The upper-state potential is obtained by adding the difference potential and the ground-state potential (Ref. 22). The parameters marked with an asterisk have been adjusted to give a difference potential that is continuous with a continuous first derivative at 8.0 Å.

	Potential parameters[a]		
Excited state:	$6p[\frac{1}{2}]_0$	$6p[\frac{3}{2}]_2$	$6p[\frac{5}{2}]_2$
This work			
$\Delta C_5(10^5\ \mathrm{cm^{-1}\,Å^5})$	0.0	−4.09±0.4	−2.98±0.3
$\Delta C_6(10^6\ \mathrm{cm^{-1}\,Å^6})$	−8.94±1.2	−8.94*	−8.94*
$\Delta C_8(10^8\ \mathrm{cm^{-1}\,Å^8})$	−21.749*	−25.693*	−15.845*
$\Delta C_{10}(10^{10}\ \mathrm{cm^{-1}\,Å^{10}})$	11.990*	14.654*	9.752*
$\Delta D_0(\mathrm{cm^{-1}})$	−22 710.460	−3334.976 8	−17 592.135
$\Delta D_1(\mathrm{cm^{-1}\,Å^{-1}})$	20 592.003	1966.574 3	15 559.894
$\Delta D_2(\mathrm{cm^{-1}\,Å^{-2}})$	−7 773.579 1	−477.594 60	−5 749.982 9
$\Delta D_3(\mathrm{cm^{-1}\,Å^{-3}})$	1 554.368 8	57.876 991	1 127.409 1
$\Delta D_4(\mathrm{cm^{-1}\,Å^{-4}})$	−173.398 18	−3.482 3146	−123.471 53
$\Delta D_5(\mathrm{cm^{-1}\,Å^{-5}})$	10.228 169	0.083 4882	7.157 7992
$\Delta D_6(\mathrm{cm^{-1}\,Å^{-6}})$	−0.249 1885	0.0	−0.171 5688
$C_5(10^5\ \mathrm{cm^{-1}\,Å^5})$	0.0	−4.09±.4	−2.98±0.3
$C_6(10^6\ \mathrm{cm^{-1}\,Å^6})$	−10.4±1.2	0.0	0.0
Gornik *et al.*			
$C_5(10^5\ \mathrm{cm^{-1}\,Å^5})$	0.0	0.0	0.0
$C_6(10^6\ \mathrm{cm^{-1}\,Å^6})$	−20.0±4.	−25.0±4.6	−27.0±4.8

[a]The difference potential has the form

$$\Delta V(R)=\frac{\Delta C_5}{R^5}+\frac{\Delta C_6}{R^6}+\frac{\Delta C_8}{R^8}+\frac{\Delta C_{10}}{R^{10}},\quad R\geq 8.0\ \text{Å}$$

$$\Delta V(R)=\sum_{n=0}^{6}\Delta D_n R^n,\quad R\leq 8.0\ \text{Å}\ .$$

tribution of both bound and free states is replaced by a classical distribution function based on the ground-state potential $V_g(R)$. For sufficiently low perturber densities the nearest-neighbor approximation may be used[21] to calculate the distribution of absorber-perturber distances. If $W(R)dR$ represents the probability that the nearest-neighbor distance is between R and $R+dR$ then

$$W(R)dR=4\pi R^2 n_0 \exp\left[\frac{-V_g(R)}{kT}\right]\times\exp\left[-4\pi n_0\int_0^R r^2\exp\left[\frac{-V_g(R)}{kT}\right]dr\right]dR\ . \tag{7}$$

The classical Franck-Condon principle may be applied to these pairs of atoms to calculate the absorption spectrum. The transition rate in this approximation is given by

$$R_{ge}=\frac{6I^2}{2\pi c\Delta\nu_1}\sum_i\sum_j\frac{2\alpha_0}{c^4\nu_{gi}(R_j)\nu_{ie}(R_j)[\nu_1-\nu_{gi}(R_j)]^2}\times W(R_j)\left[\frac{d\,\Delta V(R_j)}{d\,R_j}\right]^{-1}. \tag{8}$$

The laser linewidth $\Delta\nu_1$, the ground to intermediate frequency $\nu_{gi}(R_j)$, intermediate to excited frequency $\nu_{ie}(R_j)$, difference potential $\Delta V(R_j)$, and laser frequency ν_1 are all now expressed in units of $\mathrm{cm^{-1}}$. The internuclear separation R_j is obtained by solving the equation $\Delta V(R)=V_e(\infty)-\nu_1$; the summation is required if more than one value of R satisfies this equation. The two-photon coefficient has been expressed as a frequency-independent term α_0 divided by a very slowly varying frequency-dependent term. The mentioned frequency dependence is derived from energy detuning considerations. The potentials for the 0_u^+ and 1_u states dissociating to the 6s states that were reported by Castex[1] have been used to calculate $\nu_{gi}(R)$ and $\nu_{ie}(R)$. The effect of both the

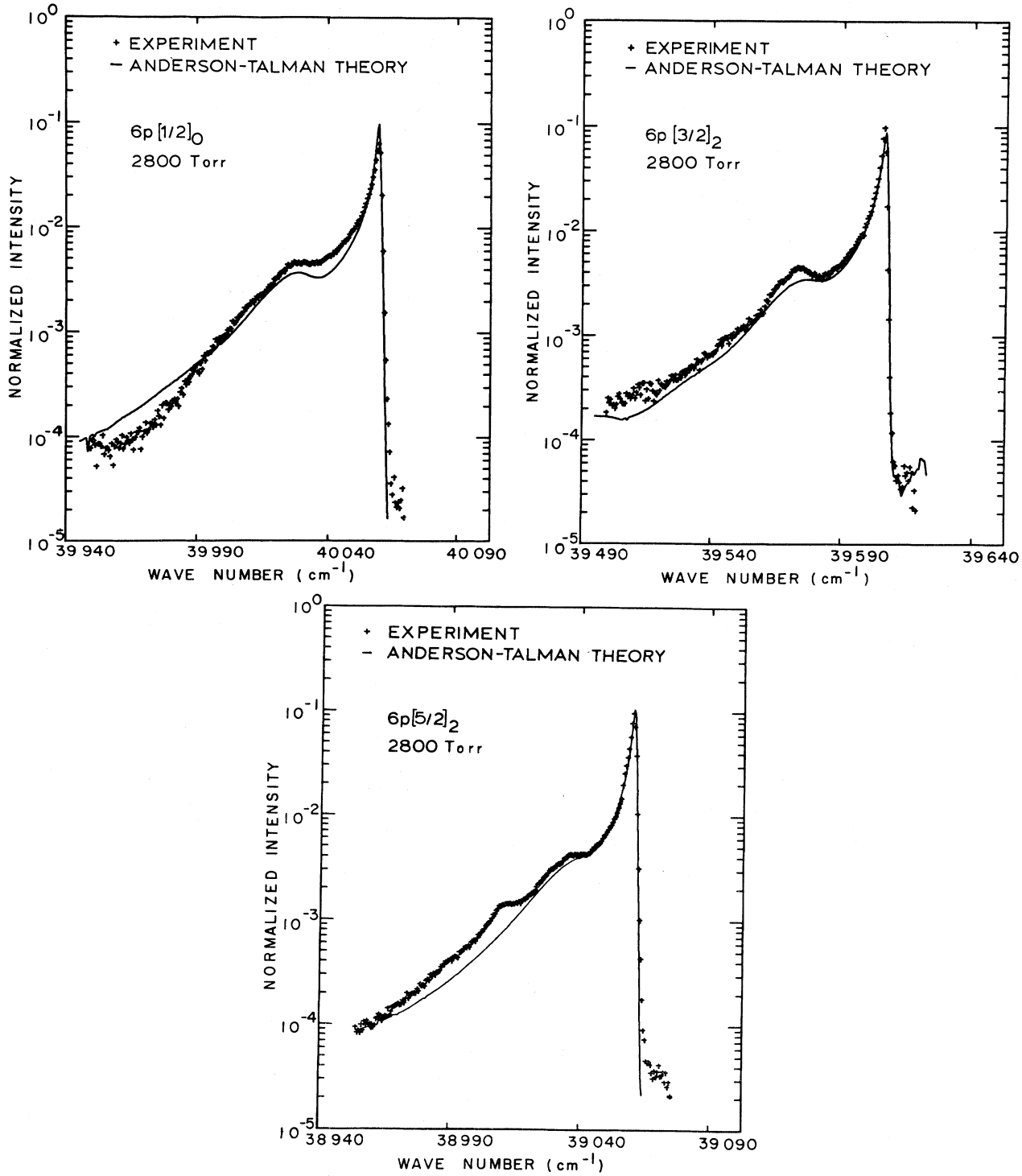

FIG. 10. High-pressure excitation spectra taken at 2800 Torr are shown in this figure. These spectra were obtained by scanning the broadband laser while monitoring the fluorescence at 1730 Å and were normalized to unit area on an atomic frequency scale. Each spectral point represents an average over at least 1500 laser shots. To reconstruct the two-photon excitation spectra, the least-squares-fit difference potential of Table II was used in an Anderson-Talman calculation (solid lines).

laser detuning and the shift in the intermediate-state energy with internuclear separation on the two-photon coefficient is small (a few percent) because of the large detuning between the laser frequency and the intermediate state. Note that the frequency-independent term α_0 has been assumed to be independent of internuclear separation. As the absorption spectrum is proportional to the inverse power of the derivative of the difference potential this theory cannot be applied near extrema in ΔV. The statistical limit of the unified Franck-Condon (uFC) treatment

of Szudy and Baylis[17] circumvents this problem. This theory uses JWKB wave functions to calculate a line shape similar to that of the quasistatic theory. The ground-state potential in both theories was represented by the potential due to Van den Biesen *et al.*[22] Both statistical theories predict the existence of satellites when the difference potential has an extremum.

The quadratic approximation[17] was used to provide first estimates of the difference potential assuming the Lennard-Jones form. This approximation yields a difference potential with a vanishing first derivative at about 9 Å and a well depth of about 80 cm^{-1}. Such potentials were found to produce spectra, under the uFC calculation, with brighter blue wings and weaker red wings than observed experimentally. The weak blue wings suggest that the difference potential is negative in the accessible range of internuclear separations. A large variety of potentials have been used in attempts to fit the spectra. In all cases difference potentials that were monotonic and negative gave the best results. By assuming that the difference potential is monotonic and negative it is possible to invert the spectrum directly by solving the equation:

$$\int_{-\infty}^{\Delta V} I(\nu)d\nu = \int_{0}^{R} W(r)dr \ , \tag{9}$$

where $I(\nu)$ is the area normalized absorption profile. This formula neglects the variation of the two-photon coefficient with internuclear separation; the effect due to the energy detuning of the intermediate states, as mentioned, is

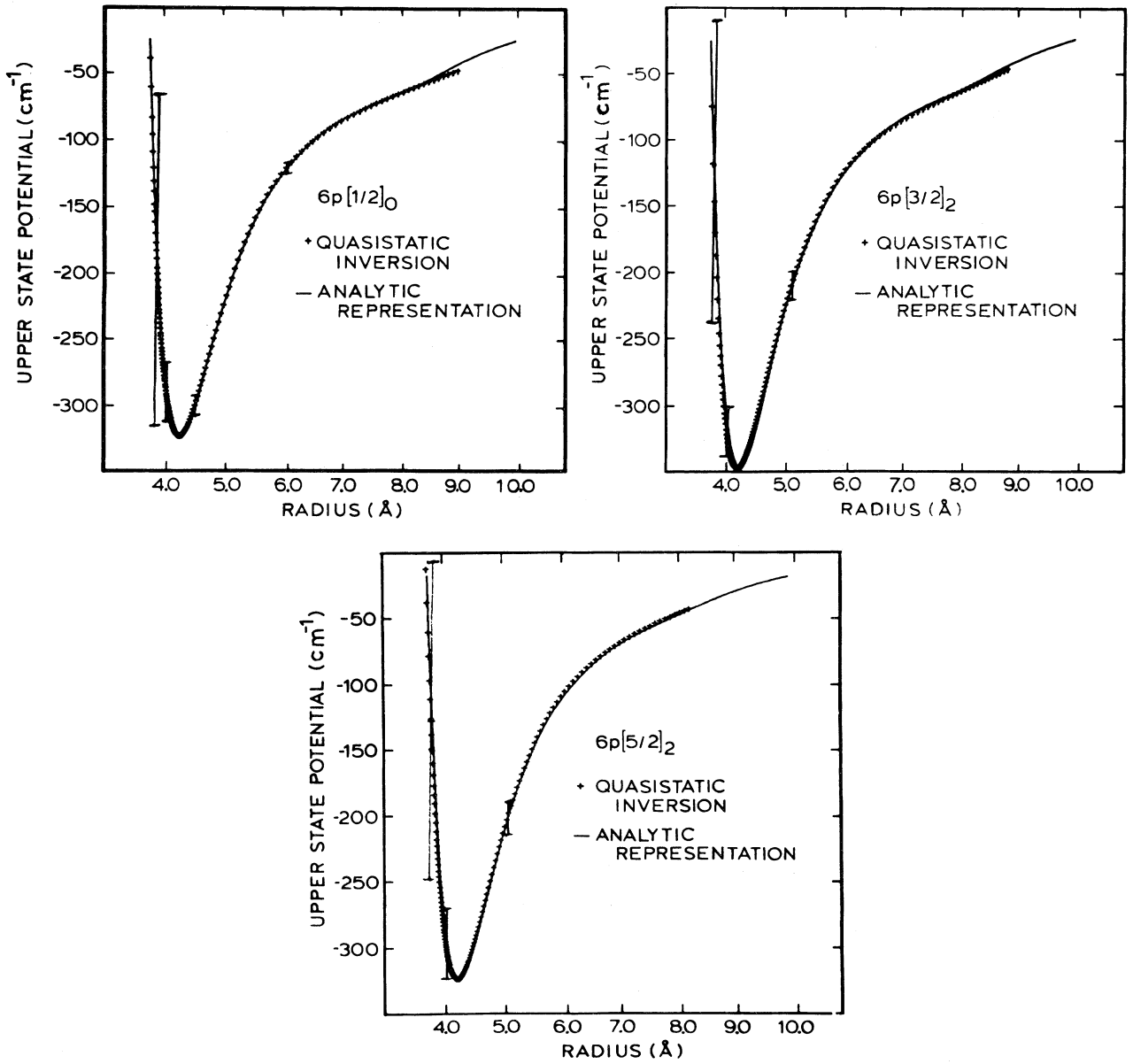

FIG. 11. This figure shows the upper-state potentials in the region of 3.75 to 10.0 Å as extracted from the 2800 Torr excitation spectra. The dots represent the values obtained by adding the ground-state potential of Van den Biesen *et al.* (Ref. 22) to the difference potentials calculated according to Eq. (9). The full drawn lines are analytic representations for which the results of the quasistatic inversion and the impact approximation were matched at 8.0 Å.

small. Solution of this equation yields the difference potential for internuclear separations from about 3.75 Å to about 10 Å. The lower limit is set by the steeply repulsive ground state and the upper limit by the requirement of the validity of the binary approximation. Figure 11 shows the upper-state potentials so derived for the three states $6p[\frac{1}{2}]_0$, $6p[\frac{3}{2}]_2$, and $6p[\frac{5}{2}]_2$. The upper-state potentials are not well described by an inverse power series.

The Anderson-Talman theory[18] has been used to treat the line shape in a unified manner. For computational ease the previously extracted difference potential was fit to a sixth-order polynomial over the range 3.75 to 8.0 Å. The long-range section was approximated using a four-term inverse power series with the leading term fixed to that measured in the impact approximation; the remaining terms were adjusted to give a potential that was smooth with continuous first derivative at 8.0 Å. For convenience, the ΔC_6 terms of the $J=2$ states were held to that measured for the $J=0$ state. The calculated spectra for all three states are shown in Fig. 10. Although line core and near wing are well described by this theory, it breaks down for large detunings from the line core due to the effect of the nonconstant ground state. For the $J=2$ states a similar algorithm was applied to extract an effective potential averaged over angular orientation. The values of the coefficients for the states $6p[\frac{1}{2}]_0$, $6p[\frac{3}{2}]_2$, and $6p[\frac{5}{2}]_2$ which gave the best fits to the data are shown in Table II. The extracted difference potentials for all three states were found to be monotonic and attractive. It should be noted that at small internuclear separations of less than 4 Å corresponding to the region of the far line wing the errors in the calculations become large due to a finite lower cutoff in the integration over frequency in Eq. (9) and due to the steepness of the ground-state potential in this region. Slight changes could cause the upper-state potentials to display a deeper minimum at separations smaller than 3.75 Å as we found previously for the $J=2$ states.[6]

Mulliken[23] estimates that $6p[\frac{1}{2}]_0$ should be repulsive (B core); however, we find that it is slightly bound ($\sim$ 320 cm^{-1}) with a minimum at $\sim$4.25 Å. Although for the $J=2$ states we expect that different potentials will be required to account for the anisotropy of the atoms, an average potential was used in the calculations and is reported here. In order to separate the contributions from the individual molecular states it is necessary to use a set of measurements with different polarizations for the laser beams.[24] The potentials for $6p[\frac{3}{2}]_2$ and $6p[\frac{5}{2}]_2$ are found to be attractive throughout the accessible region as predicted by Mulliken (A core). It should be noted that potentials with humps[23] produce line shapes with blue wings that are stronger than observed; thus, we must disagree with the assignment[5] of a potential hump to states converging towards $6p[\frac{5}{2}]_2$.

V. FLUORESCENCE SPECTRA

At high pressures we also observe line broadening in the infrared fluorescence in transitions from $5p^5 6p$ to $5p^5 6s$. The shapes of the wings of these transitions depend upon both the upper and lower potential curves of both gerade and ungerade symmetry. Since the fluorescent transitions involve a multitude of possible transitions to the lower states, $J=1$ ($\Omega=1,0$) and $J=2$ ($\Omega=2,1,0$), it would be difficult to extract potentials from these transitions. We do note in comparing transitions from *all* upper levels that transitions to $6s[\frac{3}{2}]_1$ show distinct blue wings, while transitions to $6s[\frac{3}{2}]_2$ do not (see Fig. 12).

The fluorescence spectra following two-photon excitation have been measured in the vuv and the ir. At low pressures, fluorescence is observed only from states excited by the laser or from states excited by optical cascade. As the pressure is increased, collisional deactivation populates new product states. The branching ratios are measured by tuning the laser onto the peak of the atomic resonance of the atomic pumped state and scanning the ir monochromator sequentially through the fluorescence lines of each product state. At each line, the integrated fluorescent intensity in the ir was measured relative to the fluorescence in the vuv. The latter signal monitors the two-photon excitation rate and is constant during the measurement of the product intensities. This procedure eliminates possible errors due to slight changes in the laser frequency and is equivalent to measuring the intensity of all product states simultaneously. The observed fluorescent intensities are corrected for the relative efficiency of the monochromator and detector system. Fluorescence from $6p[\frac{1}{2}]_1$ was not observable because of the limited spectral response of the RCA 8852 photomultiplier. Through the use of the radiative branching fractions of Ref. 25, the measured intensities may be related to the

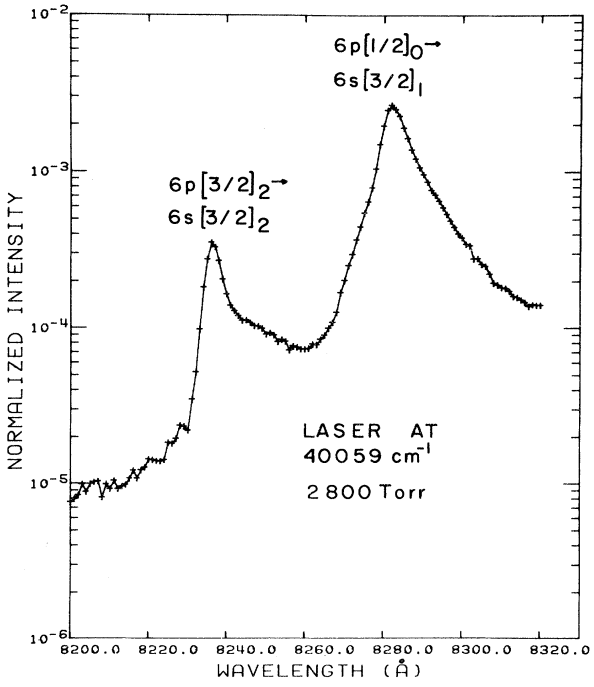

FIG. 12. Fluorescence spectrum, observed around 8230 Å, resulting from the laser excitation of $6p[\frac{1}{2}]_0$ at a pressure of 2800 Torr is shown. The $6p[\frac{3}{2}]_2$ state is collisionally excited. The figure serves to illustrate the general observation that transitions from the $6p$ manifold members to $6s[\frac{3}{2}]_1$ show distinct blue wings while transitions to $6s[\frac{3}{2}]_2$ do not.

populations of the individual states under the assumption that quenching from the product states is small. The extracted populations, normalized to the total of the observed populations, are reported in Table III from measurements taken at 100 Torr. It should be noted that intermultiplet quenching from the $6p$ manifold members is to be expected[26] and that time-dependent studies are required to extract the actual quench rates from these states.

VI. DISCUSSION OF RESULTS

We have sketched in Fig. 13 estimates for the gerade interatomic potentials based upon the potentials extracted from line broadening, expected correlations described by Mulliken,[23] and from known molecular structures. The solid heavy curves are those extracted from line-shape measurements. The dashed curves are estimates based on Mulliken's predictions and on analogies drawn from the states measured. We show a repulsive barrier for the bound states dissociating to $6p[\frac{5}{2}]_3$ as indicated by Mulliken while the B-core states correlated with $6p[\frac{3}{2}]_1$ are derived from analogy to the $6p[\frac{1}{2}]_0\ 0_g^+$ state. This feature does help explain the branching fractions reported in Table III as we shall explain.

At each avoided crossing in the diabatic curves shown in Fig. 13 we have placed a dot. Large couplings may be expected between the curves at these points. There are no repulsive curves of "gerade" $6p$ states crossing $6p[\frac{1}{2}]_0$ for internuclear separations greater than 3.75 Å. Intramultiplet deactivation of $6p[\frac{1}{2}]_0$ to other $6p$ levels could then proceed by a double crossing, first to attractive states from $5p^5 5d$ and then again to repulsive states of $5p^5 6p$. This accounts for the small branching fractions observed (Table III). Based on calculations of excited-state potentials[27] we suggest that crossings to 0_g^+ and 1_g states of $6s'[\frac{1}{2}]_1$ occur at large internuclear separations. This would imply that substantial intermultiplet deactivation could take place. Preliminary lifetime measurements confirm this in that the total quench rate of $6p[\frac{1}{2}]_0$ is larger than the deexcitation rate to all the other $6p$ levels as inferred from the measured branching fractions. In Fig. 13,

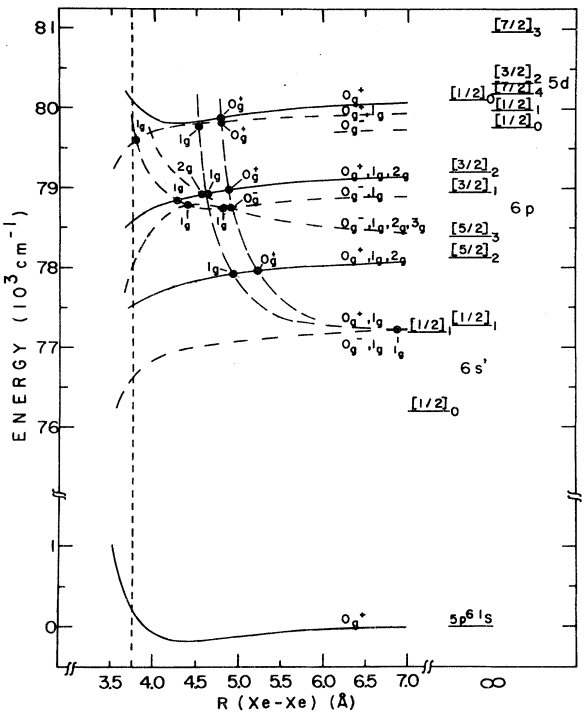

FIG. 13. Gerade molecular curves relevant to this work are plotted in this figure. The heavy solid lines are those potentials extracted from this work, while the dashed curves are estimated. Avoided crossings are indicated with dots.

the large branching fractions from $6p[\frac{3}{2}]_2$ to $6p[\frac{5}{2}]_3$ can be explained by crossings with $6p[\frac{3}{2}]_1(1g)$ and $6p[\frac{5}{2}]_3(2g)$. The repulsive barrier brings both attractive and repulsive states near in energy to weakly attractive potentials; hence, the $1g$ symmetry of $6p[\frac{3}{2}]_1$ may have strong coupling to the attractive $1g$ symmetry of $6p[\frac{3}{2}]_3$ near the vicinity of the barrier. This would explain why the branching fractions from any of the states to $6p[\frac{3}{2}]_1$ are the smallest and to $6p[\frac{5}{2}]_3$ the largest. Any energy

TABLE III. Measured branching fractions for population by intramultiplet collisional deactivation of the laser excited state. The fluorescence spectrum following selective excitation of one of the two-photon accessible states has been used to give a measure of the population of states excited via collisions. The branching fractions are quoted for a pressure of 100 Torr under the assumption that the quench rates of the product states are small compared to their radiative rates. Entries with — — — had intensities that were too weak to measure. The values are normalized to sum to one.

Laser excited state:	Branching fractions $6p[\frac{1}{2}]_0$	$6p[\frac{3}{2}]_2$	$6p[\frac{5}{2}]_2$
Collisionally excited states		Branching fractions	
$6p[\frac{1}{2}]_0$	0.94±0.03	— — —	0.001±0.0002
$6p[\frac{3}{2}]_2$	0.018±0.01	0.63±0.03	0.0042±0.0016
$6p[\frac{3}{2}]_1$	0.0052±0.0026	0.025±0.004	0.001±0.0005
$6p[\frac{5}{2}]_3$	0.027±0.003	0.27±0.015	0.24±0.013
$6p[\frac{5}{2}]_2$	0.0085±0.0048	0.078±0.015	0.76±0.077

transferred to repulsive states of $6p[\frac{3}{2}]_1$ is, in turn, likely to be transferred to $6p[\frac{5}{2}]_3$ before the state dissociates. In Table III, a surprising result is the large collisional excitation found from $6p[\frac{5}{2}]_2$ to higher excited levels. The branching ratios listed in Table III include influences due to the ungerade molecular states as well as the gerade states. A complete explanation of the observed ratios is not possible without further information and, in particular, a study of the time dependence is necessary.

We have explored several possible interpretations for the spectral feature near 39 800 cm^{-1} in Fig. 5. This feature has been observed by Gornik and co-workers[5] at pressures as low as 28 Torr. We have measured the pressure dependence at the peak of this band to be identical to the quasistatic line wing of $6p[\frac{1}{2}]_0$. This indicates that the feature originates from two-photon transitions of pairs (collision induced). The shape suggests a red satellite of $6p[\frac{1}{2}]_0$; although this would seem to cause an unreasonably deep well for this state, which is predicted to be repulsive.[23] The only other spectral features in the region between $6p[\frac{1}{2}]_0$ and $6p[\frac{3}{2}]_2$ are $5d[\frac{1}{2}]_0$, expected at 39 886 cm^{-1} in Fig. 5, and $5d[\frac{1}{2}]_1$ at 39 997 cm^{-1}. The former does not have an allowed dipole-quadrupole transition and though the latter could, none is visible at these energies in Fig. 5 or in the higher resolution scans of Fig. 10. Castex[1] has observed transitions to 0_u^+ or 1_u symmetries of $5d[\frac{1}{2}]_1$ with a red satellite. This satellite is expected at 39 900 cm^{-1} in Fig. 5. (Perhaps dipole-quadrupole transitions to these symmetries are forbidden with linearly polarized light, but can be induced by collisions.) These shallow wells[1] are caused by crossings with the 1_u repulsive curve of $6p[\frac{3}{2}]_1$ from below. As shown in Fig. 13, similar crossings occur for the 1_g symmetries of these states. Hence, the feature could be attributed to collision-induced dipole-quadrupole transitions in the red wing of $5d[\frac{1}{2}]_1(1_u)$ or to collision-induced dipole-dipole transitions to the blue wing of $6p[\frac{3}{2}]_1(1_g)$. The latter interpretation seems to agree better with the frequency observed in Fig. 5.

To test if bound states of $5d[\frac{1}{2}]_1$ are involved, we searched for excimer fluorescence in the red wings of the $5d[\frac{1}{2}]_1 \rightarrow {}^1S_0$ transition at 119 nm while exciting at 39 800 cm^{-1}. No fluorescence was observed. In the ir, excimer fluorescence was observed from $6p[\frac{3}{2}]_2$ with a branching fraction for the $6p$ manifold of 0.32 ± 0.20 and from $6p[\frac{3}{2}]_3$ with a branching fraction of 0.68 ± 0.14. No fluorescence was observed from other states of the $6p$ manifold. This result contradicts an interpretation as a red satellite of $6p[\frac{1}{2}]_0$ and strongly suggests that excitation at 39 800 cm^{-1} produces dissociative states of $6p[\frac{3}{2}]_1$ which couple to $6p[\frac{3}{2}]_2$ and $6p[\frac{5}{2}]_3$ as the nuclei separate.

ACKNOWLEDGMENTS

We are indebted to John Kielkopf for his assistance and advice in the development of the Anderson-Talman lineshape code. We also wish to thank M. C. Castex, W. E. Baylis, R. J. Bieniek, and L. Frommhold for fruitful discussions. This work was supported by the U.S. Department of Energy (Office of Basic Energy Sciences) and the Robert A. Welch Foundation.

---

*Present address: Sandia National Laboratories, Albuquerque, NM 87185.

†Present address: AT&T Bell Telephone Laboratories, 600 Mountain Ave., Murray Hill, NJ 07974.

[1]M. C. Castex and N. Damany, Chem. Phys. Lett., 24, 437 (1974); M. C. Castex, Chem. Phys. 5, 448 (1974); J. Chem. Phys. 74, 759 (1981); L. Laporte, J. L. Subtil, and M. C. Castex, in *Spectral Line Shapes* (de Gruyter, Berlin, New York, 1983), Vol. 2, p. 583.

[2]R. Broadman and G. Zimmerer, J. Phys. B 10, 3395 (1977).

[3]A. Margani, C. Nguyen Xuan, G. Di Stefano, and M. Lenzi, J. Chem. Phys. 70, 2871 (1979).

[4]R. T. Hawkins, H. Egger, J. Bokor, and C. K. Rhodes, Appl. Phys. Lett. 36, 391 (1980).

[5]W. Gornik, S. Kindt, E. Matthias, H. Rinneberg, and D. Schmidt, Phys. Rev. Lett. 45, 1941 (1980); W. Gornik, S. Kindt, E. Matthias, and D. Schmidt, J. Chem. Phys. 75, 68 (1981); W. Gornik, E. Matthias, and D. Schmidt, J. Phys. B 15, 3413 (1982).

[6]N. Böwering, Chien-Yu Kuo, T. D. Raymond, and J. W. Keto, in *Spectral Line Shapes* (de Gruyter, Berlin, New York, 1983), Vol. 2, p. 927.

[7]J. W. Keto, T. D. Raymond, and S. T. Walsh, Rev. Sci. Instrum. 51, 42 (1980).

[8]T. D. Raymond, S. T. Walsh, and J. W. Keto (unpublished).

[9]A. Yamagishi and A. Szabo, Appl. Opt. 16, 691 (1977).

[10]A. W. McCown, M. N. Ediger, and J. G. Eden, Phys. Rev. A 26, 2281 (1982).

[11]M. Stockton, J. W. Keto, and W. A. Fitzsimmons, Phys. Rev. A 5, 372 (1972).

[12]G. Grynberg and B. Cagnac, Rep. Prog. Phys. 40, 791 (1977).

[13]J. D. Jackson, *Classical Electrodynamics,* 2nd ed. (Wiley, New York, 1975).

[14]C. H. Chen, G. S. Hurst, and M. G. Payne, Chem. Phys. Lett. 75, 473 (1980).

[15]M. S. Pindzola, M. G. Payne, and W. R. Garrett, Phys. Rev. A 24, 3115 (1981).

[16]Nicole Allard and John Kielkopf, Rev. Mod. Phys. 54, 1103 (1982).

[17]J. Szudy and W. Baylis, J. Quant. Spectrosc. Radiat. Transfer 15, 641 (1975); 17, 681 (1977).

[18]P. W. Anderson and J. D. Talman, Bell Teleph. Syst. Tech. Publ. 3117, 1 (1956).

[19]H. Margenau, Rev. Mod. Phys. 8, 22 (1939).

[20]J. A. Barker, M. L. Klein, and M. V. Bobetic, IBM J. Res. Dev. 20, 222 (1976).

[21]S. Chandrasekar, Rev. Mod. Phys. 15, 1 (1943).

[22]J. J. H. Van den Biesen, F. A. Stokvis, E. H. van Veen, and C. J. van den Meijdenberg, Physica (Utrecht) A100, 375 (1980).

[23]R. S. Mulliken, J. Chem. Phys. 52, 5170 (1970); Radiat. Res.

59, 357 (1974).
[24]W. M. McClain, J. Chem. Phys. 55, 2789 (1971).
[25]H. Horiguchi, R. S. F. Chang, and D. W. Setser, J. Chem. Phys. 75, 1207 (1981).
[26]J. Sabbagh and N. Sadeghi, J. Quant. Spectrosc. Radiat. Transfer 17, 297 (1977).
[27]W. C. Ermler, Y. S. Lee, K. S. Pitzer, and N. W. Winter, J. Chem. Phys. 69, 976 (1978).